In-situ radiation response of additively manufactured modified Inconel 718 alloys

E. Aydogan[1,], O. El-Atwani[2], B. Erdem[1], W-Y. Chen[3], M. Li[3], A. Devaraj[4], B. Koc[5], S.A. Maloy[2]*

[1] Middle East Technical University, Ankara, 06800, Turkey

[2] Los Alamos National Laboratory, Los Alamos, NM 87544, USA

[3] Division of Nuclear Engineering, Argonne National Laboratory, Argonne, IL, USA

[4] Physical and Computational Sciences Directorate, Pacific Northwest National Laboratory, Richland, WA, USA

[5] Integrated Manufacturing Center, Sabanci University, Istanbul, 34906, Turkey

Abstract: In this study, a novel alloy of modified Inconel 718 which is produced by selective laser melting technique is studied before and after in-situ Kr irradiation up to 3 dpa at 200 and 450 °C. Before irradiation, the microstructure consists of dislocation cells having a misorientation angle less than 5° and with an average size of ~500 nm. There are also second phase particles of MC type carbides, Laves phase and oxides such as Y-O, Y-(Ti)-Al-O. While the microstructure consists of stacking fault tetrahedras, faulted and perfect loops after irradiation at 200 °C, dislocation loops are the primary defects at 450 °C. With increasing dose, the size of the defects remains similar at 200 °C while it increases at 450 °C. This has been attributed to the existence of vacancy type defects at 200 °C and the different defect transport mechanisms at different temperatures. Moreover, matrix and second phase particle compositions seem to be similar after irradiation. The sink strengths of the structures have been calculated and superior radiation resistance of this alloy has been attributed to the existence of fine cell boundaries stabilized by the second phase particles produced by additive manufacturing.

Key Words: Selective laser melting, modified Inconel 718, in-situ irradiation, radiation induced defects, cellular structure

Introduction:

Structural materials are required in-core components of Gen IV reactors which are designed to operate at doses ranging from tens to hundreds of dpa at temperatures up to ~900 ºC [1, 2]. Nickel based superalloys have been considered for Gen IV in-core components due to their excellent corrosion resistance and creep properties compared to austenitic and ferritic/martensitic steels [2, 3]. High Ni content of these alloys is the source of resistance to radiation induced swelling, thus radiation resistance is another remarkable property of nickel-based superalloys [4]. These properties were attributed to the existence of long-range order spherical shaped γ' (Ni_3(Al, Ti)) precipitates with face centered cubic (FCC) crystal structure and disk-shaped γ'' (Ni_3Nb) with body centered tetragonal (BCT) crystal structure [1]. On the other hand, these precipitates have been reported to be unstable – either disordering and/or

*Corresponding author.
E-mail address: aydogane@metu.edu.tr

dissolution occurs – under irradiation. For instance, Sencer et al. have reported that γ' and γ'' precipitates disordered under proton irradiation at the doses as low as 0.6 dpa at the temperature range of 32-55 ^{o}C in Inconel 718 alloys [5]. Moreover, Sun et al. have studied the stability of γ' precipitates in Rene N4 Ni-based superalloys and found a complete disordering of γ' precipitates at a dose of 0.3 dpa and partial dissolution at the dose of 75 dpa at room temperature. It has been discovered that disordering of these particles results in loss in strength [6]. Moreover, dissolution of the precipitates at higher doses can lead to an increase in damage accumulation due to the reduction in interfaces acting as defect sinks [7].

Oxide dispersion strengthened (ODS) alloys have been shown to exhibit outstanding radiation resistance and mechanical properties at much higher temperatures due to the existence of nano-oxide particles which are reported to be mostly, Y-Ti-O, YAG, YAH [8-11]**.** These particles can stabilize the microstructure by pinning the grain boundaries and dislocations, and act as sinks for the point defects that result from irradiation [12-14]. Conventionally, these alloys are produced by powder metallurgy techniques including several steps, such as ball milling, hot consolidation processes and heat treatment. Even though nano-structures with high density of nano-oxide particles ($>10^{23}$ m^{-3}) have been achieved, these processing methods are quite time intensive and expensive [9, 15]. Additive manufacturing (AM) has recently been an attractive alternative for fabrication of complex shaped and fully dense parts layer by layer with materials that are difficult to process with conventional techniques [16]. Moreover, waste of materials is reduced, and intermediate steps used in conventional production techniques are eliminated with the AM technologies [17, 18]. Therefore, additive manufacturing has become an attractive technique to construct nuclear reactor components, such as fuel rods, cladding tubes and hexagonal ducts [19]**.**

Among additive manufacturing technologies, laser powder bed fusion (LPBF) process, also called selective laser melting (SLM) is a widely used fabrication method due to high dimensional accuracy and good surface integrity of manufactured parts [3, 16]. Recently, Chen et al. produced CoCrFeMnNi high entropy alloys with Mn oxide using LPBF where oxygen is picked up from the atmosphere and the feedstock particles. The particles are shown to be relatively coarse, with an average size of ~100 nm [20]. Similarly, Qiu et al. [21] have produced Fe-Ni alloy with Fe_3O_4 oxides using SLM technique while Tan et al. [22] have produced nickel-based ODS alloys using mechanical alloying and laser metal deposition, and reported an average of oxides >100 nm. Moreover, Shi et al. produced Fe-9Cr ferritic alloys with a reasonably high number density of oxides having sizes <20 nm using laser engineered net shaping (LENS) and hot isostatic pressing. As-built samples were reported to have low densifications and therefore hot consolidation was required [23]. Even though these studies clearly show a promise to obtain ODS alloys with AM processes, it has been a big challenge to control the size and distribution of the oxide particles using AM techniques, especially without mechanical alloying and hot consolidation after production.

In this study, Inconel 718 composition has been modified to obtain high density of second phase particles for improved radiation response. Moreover, for the first time, this grade of modified nickel-based alloy has been additively manufactured using selective laser melting technique. We present here the microstructure of this materials and its irradiation response during in-situ TEM-irradiation experiments in as-built condition. We demonstrate that the initial microstructure consists of high density of dislocation cells and second phase particles.

Irradiations on these alloys at 200 °C and 450 °C up to 3 dpa result in much less damage compared to the other nickel-based alloys. Besides, there is no considerable segregation/depletion and radiation induced precipitation. The improved radiation resistance of this alloy has been attributed to the formation of cell structure stabilized by the second phase particles. Thus, this study clearly shows the promise of additively manufactured Inconel alloys for the nuclear applications.

1. Experimental procedure:

1.1. Production of alloys

A new grade of Ni-based superalloys has been produced by mixing the Inconel 718 (IN-718) powders with Y_2O_3 nano-powders (18-38 nm) and Ti6Al-4V powders manually to obtain IN-718-0.2 wt.% Y_2O_3-0.5 wt.% Ti6Al-4V. The aim of using Ti6Al-4V is to provide an extra source of Titanium for the formation of Y-Ti-O particles and solid solution strengthening by Vanadium and Aluminum. IN-718 and Ti6Al-4V powders have been provided by EOS Inc. and their size ranges between 20-55 μm. The composition of powders and resultant nominal composition of the alloy measured by Energy-dispersive X-ray spectroscopy (EDS) have been provided in Table 1. Alloys were manufactured by selective laser melting technique (EOS M290, EOSINT GmbH-Electro Optical system, Germany), with 300 W laser power, 1000 mm/s scan speed, 40 μm layer thickness and 110 μm hatch distance. 10x10x5 mm^3 blocks were produced using scanning strategy of 67° rotation on a stainless steel base plate.

Table 1: Chemical composition of IN-718 and Ti6Al-4V powders and nominal composition of the resultant alloy (in wt.%).

Elements	**IN 718**		**Ti6Al-4V**		**Resultant composition**
	Min	**max**	**min**	**max**	
Ni	50	55	-		48.3
Cr	17	21	-		19.6
Fe	Balanced		≤0.3		17.5
Nb	4.75	5.5	-		4.6
Mo	2.8	3.3	-		2.4
Ti	0.65	1.15	Balanced		2.0
Al	0.2	0.8	5.5	6.75	2.0
Co	≤1		-		≤1
Cu	≤0.3		-		≤1
Si	≤0.35		-		1.0
Mn	≤0.35		-		0.4
V			3.5	4.5	0.4

1.2. In-situ irradiation experiments

In-situ irradiations were conducted at 200 °C and 450 °C up to $1.6x10^{15}$ ions/cm^2 fluence corresponding to 3 dpa using 1 MeV Kr ions at the intermediate voltage electron microscope (IVEM) at Argonne National Laboratory. Irradiation dose rate is specified to be $6.5x10^{11}$

ions/sqCm/s. Supplementary Fig. S1 shows the damage profiles calculated by Monte Carlo simulation code SRIM in Kinchin-Pease mode with a displacement energy of 40 eV [41] for ~3 dpa at the first 100 nm which is the thickness of the TEM foil.

For the investigation of defects, samples were pre-tilted to g<200> two beam conditions either from [200] or [110] zone axes. Irradiations were stopped at 0.5, 1, 2 and 3 dpa, and bright field (BF) and dark field (DF) analyses were conducted.

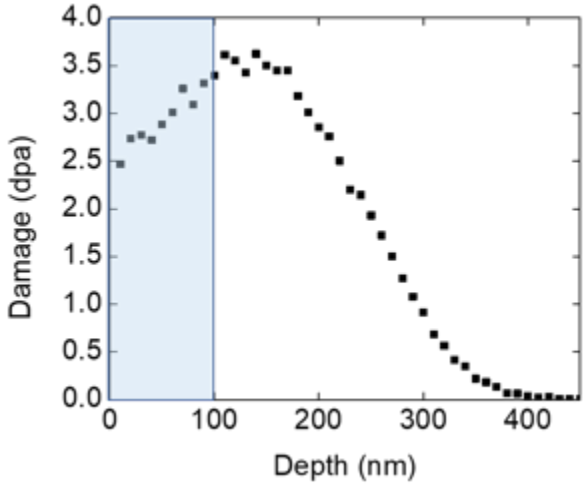

Figure S1. SRIM-calculated depth profile of damage in pure Ni irradiated with 1 MeV Kr ions to ~3 dpa within 100 nm, shown by a shaded region.

1.3. Characterization

Discs having 3-mm diameter were cut using electrical discharge machining (EDM). Electron backscatter diffraction (EBSD) and transmission electron microscopy (TEM) foils were prepared using jet electropolishing at a temperature of -30 ºC with TenuPol-5 polisher under a voltage of 20 V. Perchloric acid (HClO4) - methanol (5:95 vol%) is used as electrolytic solution.

The grain morphology of as-built sample was examined by EBSD in a FEI Inspect FEG SEM equipped with TSL EBSD detector. Experiments were conducted on the 70° pre-tilted samples at an acceleration voltage of 20 kV using an aperture size of 50 µm with a step size of 50 nm. In order to cover large enough area, scans were carried out at 75 µm x 75 µm regions.

Microstructures were examined by FEI Tecnai F30 transmission electron microscope in bright field mode at an acceleration voltage of 300 kV. Energy-dispersive X-ray spectroscopy (EDS) was used to determine the composition of the precipitates. Data collection times for each precipitate were at least 60 s in order to be able to get high peak-to-background ratios. Qualitative elemental analyses were achieved using the FEI software TIA. The size and number density of defects were measured manually using the ImageJ v1.49 digital processing software including at least 100 counts from two different location for each irradiation condition.

Needle shaped samples for atom probe tomography (APT) was fabricated by a standard lift-out and annular milling process from as-deposited and irradiated alloy using a Thermo Fisher Scientific Helios Nanolab 600 dual beam focused ion beam scanning electron microscope [24]. The APT analysis was conducted using a CAMECA LEAP 4000 XHR. For APT samples with a precipitate, the laser pulse energy was maintained at 60-100 pJ with a laser pulse repetition rate of 125KHz. The APT needles of matrix before and after irradiation was analyzed using

pulsed voltage mode with 20% pulse fraction and 200KHz voltage pulse repetition rate. The specimen temperature for all samples were maintained at 57K with a target evaporation rate of 0.005 atoms/pulse. The APT data was reconstructed using IVAS 3.8.

2. Results

Microstructure before irradiation:

In this study, Inconel-718 composition has been modified by combining IN-718, Ti6Al-4V and Y_2O_3 powders (IN-718 - 0.2 wt.% Y_2O_3 - 0.5 wt.% Ti6Al-4V) to obtain high density of second phase particle formation for improved radiation resistance. The alloy has ~0.25% porosity and a hardness of 343.2±9.1 HV. Orientation distribution of grains after SLM process is shown in Fig. 1a. Small orientation differences within the grains infers the cell formation which has been shown by the gray scale map in Fig. 1b. It is clear that the grain boundaries are mostly high angle grain boundaries (HAGBs - >15°) while the cell boundaries are low angle grain boundaries (LAGBs). Fig. 1c shows the cells within a grain which have the size of ~500 nm. They are formed by the dislocation accumulation. Dislocation density within the cells is measured as ~2.5×10^{14} m^{-2} from the TEM micrographs. Selected angle diffraction pattern along the zone axis of <100> at the inset of Fig. 1c shows no ordering which indicates the lack of γ'/ γ'' formation. In Fig. 1d TEM micrograph presents the existence of various second phase particles which have different size and shapes. They are distributed mostly at the cell boundaries while small fraction being inside the cells.

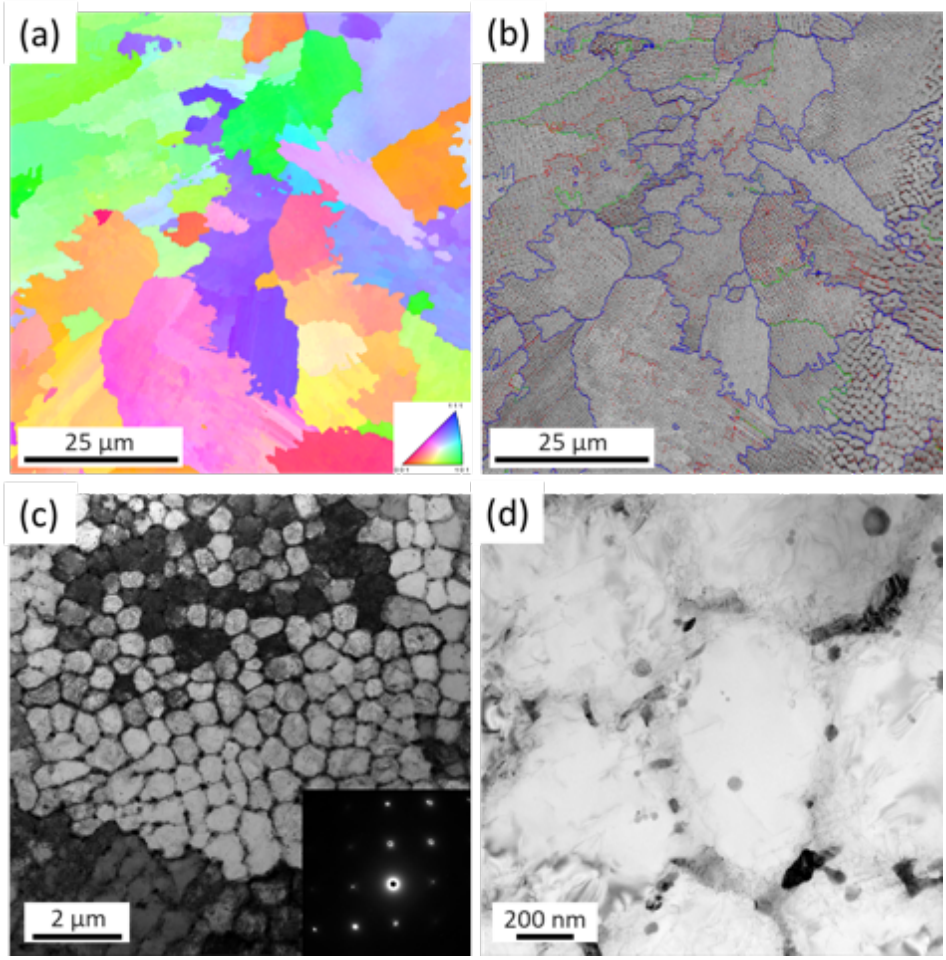

Figure 1. (a) EBSD orientation map (b) gray scale map showing the grain boundary misorientation angle (Blue > 15°; Green between 15° and 5°; Red < 5°) (c) Bright field TEM showing the cell structure within a grain (d) TEM micrograph showing the distribution of second phase particles.

Fig. 2 presents the EDX maps of the material showing composition of second phase particles. Besides mapping, point analyses have been conducted on indivudial particles. From the EDX data it is clear that particles are Mo-Nb-Ti-(V) rich carbides and Laves phase; Y-O, Y-(Ti)-Al-O; Fe-Cr-Mo-Nb-Ti-Al-V particles. Moreover, cell boundaries are slightly enriched in Ti, Nb and Mo; depleted in Fe and Cr. Overall, while the spherical particles are oxides and carbides, larger irregular shaped particles are Laves phase. Size of the (almost) spherical particles is 22.5±1.5 nm and density is $6.0\pm0.9\text{x}10^{20}$ m^{-3}.

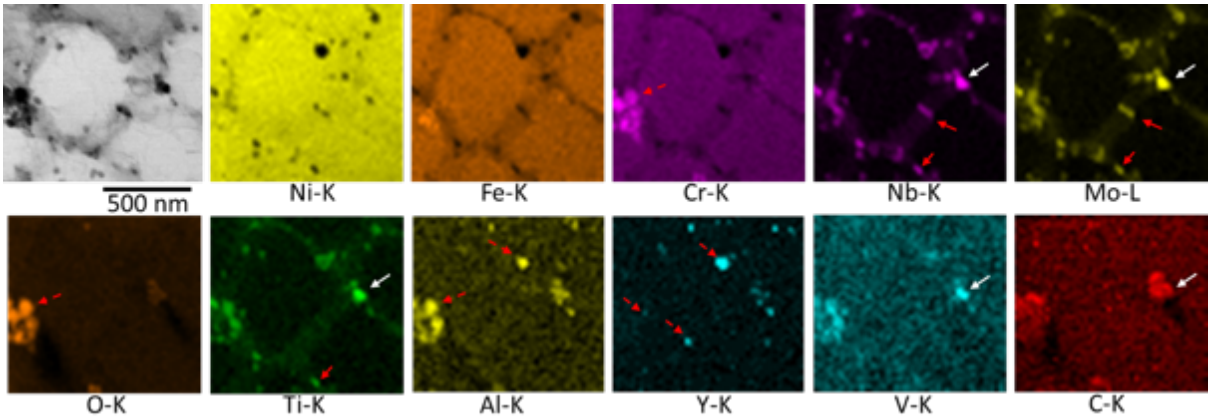

Figure 2. EDX map showing the composition of second phase particles. White and red arrows indicate some of the carbides and Laves phase, respectively. Red dashed arrows indicate different types of oxides.

Microstructure after in-situ irradiations:

In-situ irradiation is applied on the as-built samples in order to examine the radiation resistance of the samples. Samples are irradiated at 200 and 450 °C and damage accumulation is observed at 0.5, 1, 2 and 3 dpa. Figs. 3 and 4 present TEM micrographs of irradiated samples at 200 and 450 °C, respectively. It is clear that damage increases with increasing dose in both irradiation condition.

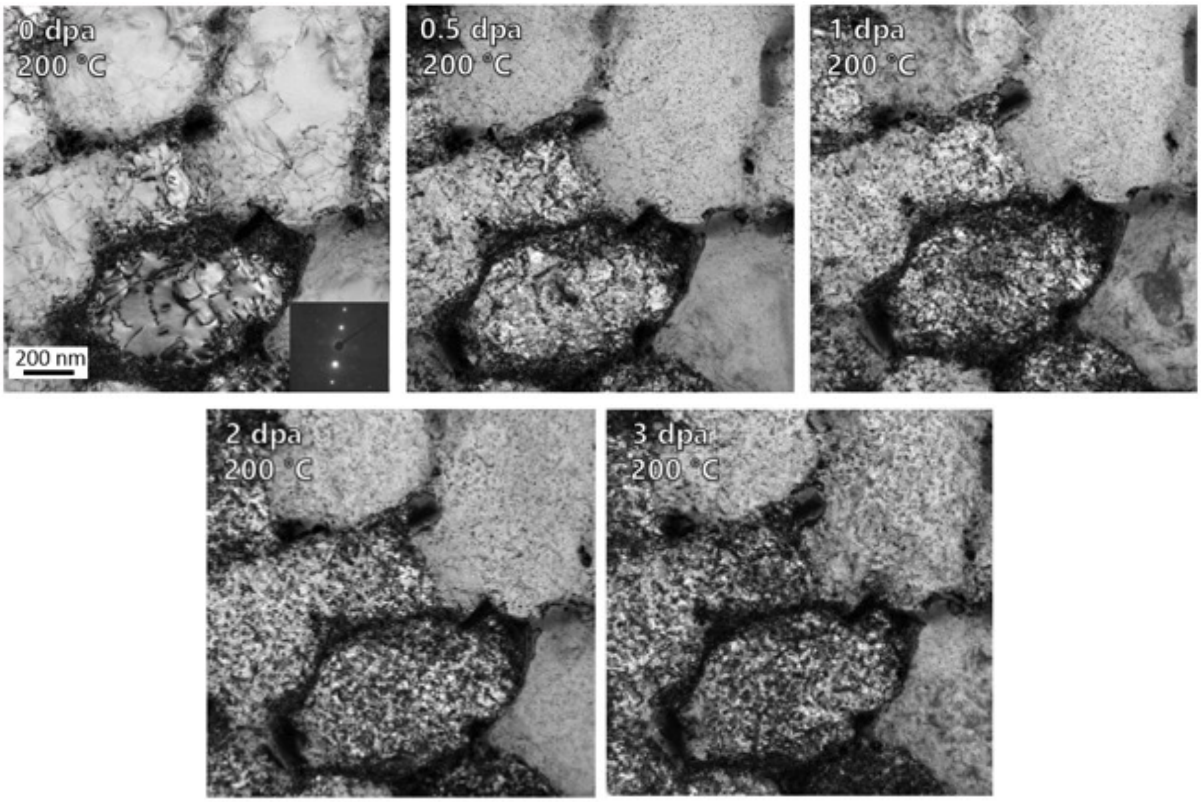

Figure 3: Bright field TEM micrographs of irradiated samples at 200 °C as a function of dpa. Images were taken at g<200>.

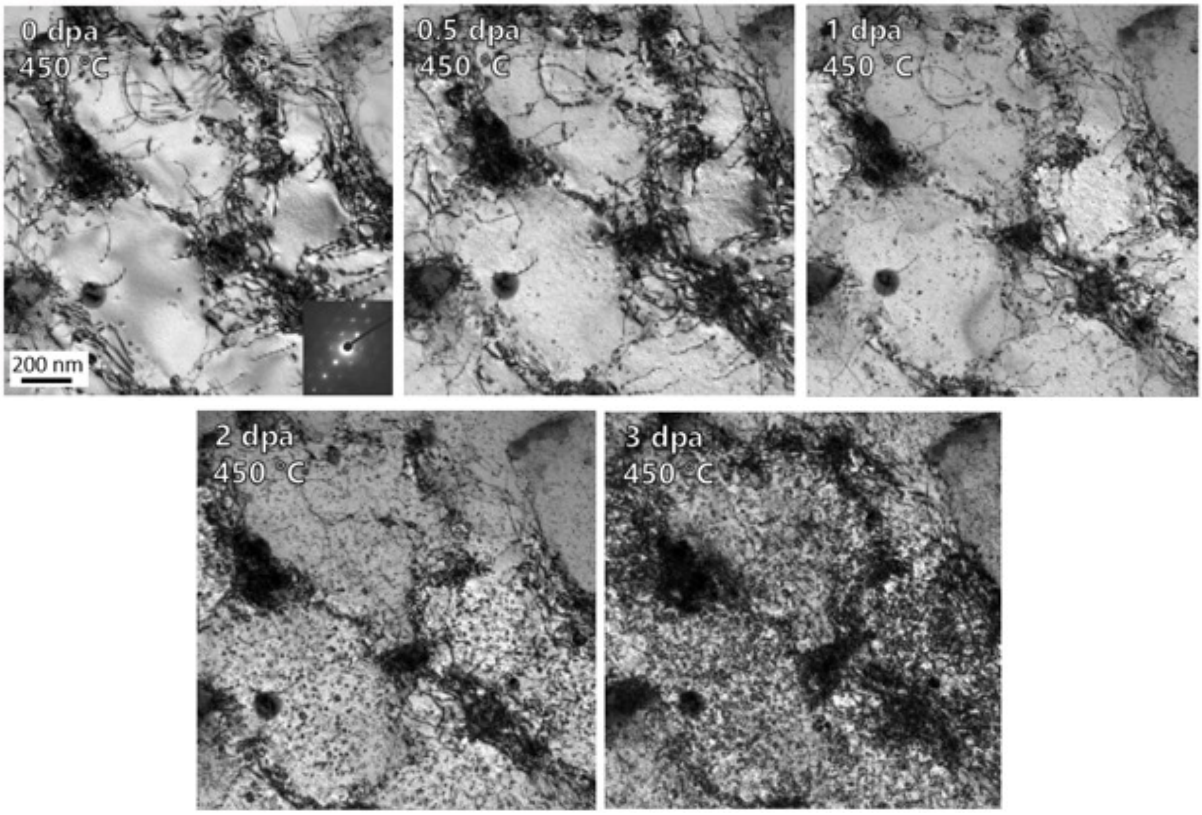

Figure 4: Bright field TEM micrographs of irradiated samples at 450 °C as a function of dpa. Images were taken at g<200>.

Assuming that damage is mostly in dislocation loops, dislocation loop area (size), areal density and damage are measured using TEM images obtained after irradiation, seen in Fig. 5. Here, damage is defined as average loop area x number of loops/area [25]. Fig. 5a shows that while the loop area remains constant ~17 nm^2 at 200 °C, it starts at ~23 nm^2, increases up to 2 dpa and remains similar (~30 nm^2) at 450 °C. On the other hand, areal loop density increases with dose at both 200 and 450 °C (Fig. 5b). However, loop density is smaller at 450 °C for all doses. It should be noted that loop density is underestimated since 2/3 of the perfect loops of a/2<110> can be detected while all the faulted loops of a/3<111> are detected along g<200>. At low doses up to 2 dpa, damage is lower at 450 °C; however, damage at 450 °C starts to surpass the one at 200 °C at and above 2 dpa, as shown in Fig. 5c. This can be attributed to the sharp increase in both loop size and loop density at 450 °C. It should also be noted that density of small defect clusters as a result of 200 °C irradiations might be underestimated due to the resolution limit of TEM.

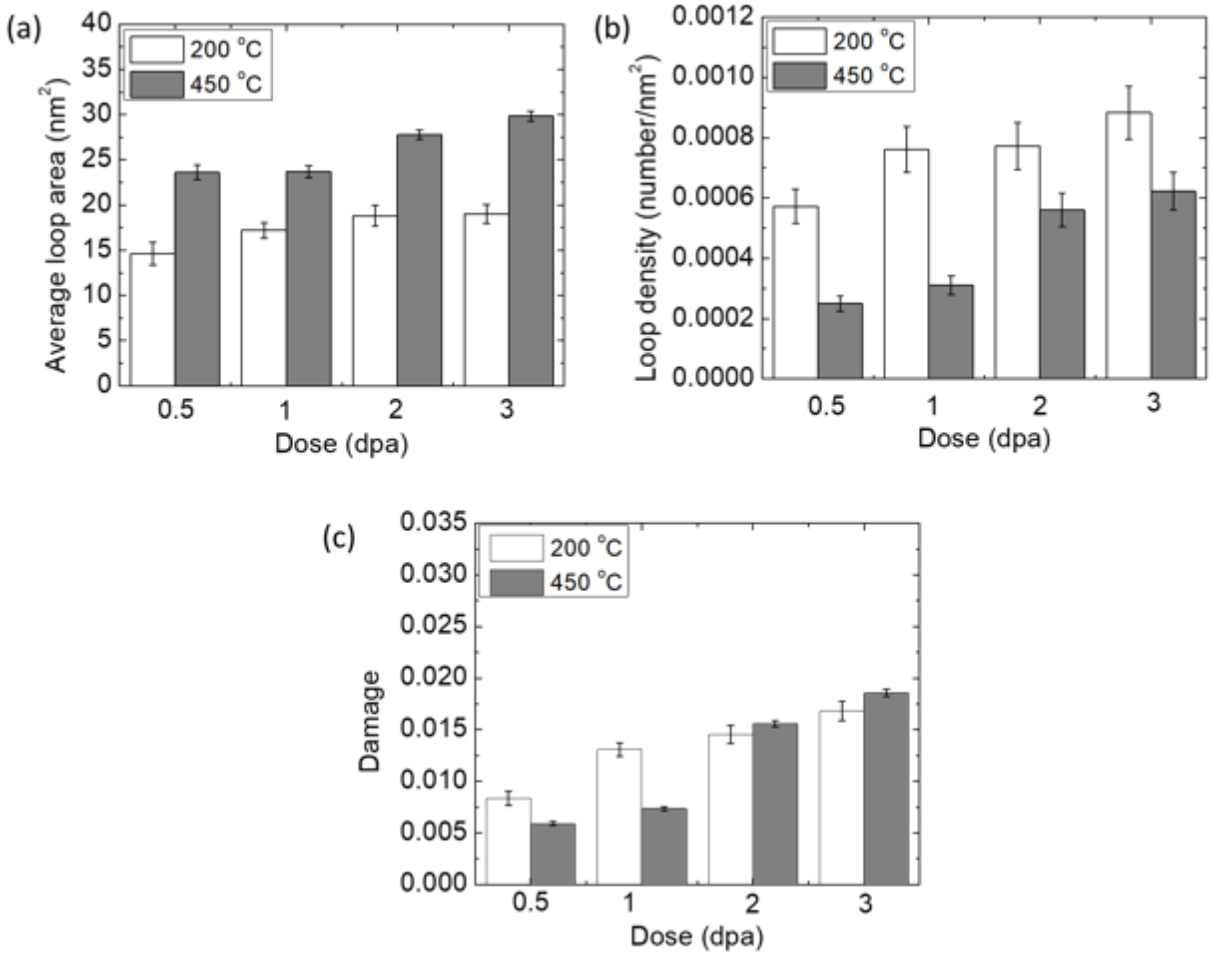

Figure 5. (a) Average loop area (size) (b) loop density and (c) damage with respect to dose at 200 and 450 °C.

In Fig. 6 APT reconstructions have indicated the existence of second phase particles after 3 dpa irradiation at 450 °C, similar to the case prior to irradiation (Fig. 2). Fig. 6a shows that there are Fe-Cr-Mo-Nb carbides after irradiation while Fig. 6b shows a particle rich in Nb,

Mo and C (MC type carbide). In other words, irradiation neither affects the pre-existing carbides nor results in second phase precipitation. On the other hand, 3D reconstructions in Fig. 6b clearly shows the enrichment of Ni, Ti and Al, and depletion of Fe and Cr at the precipitate/matrix interface.

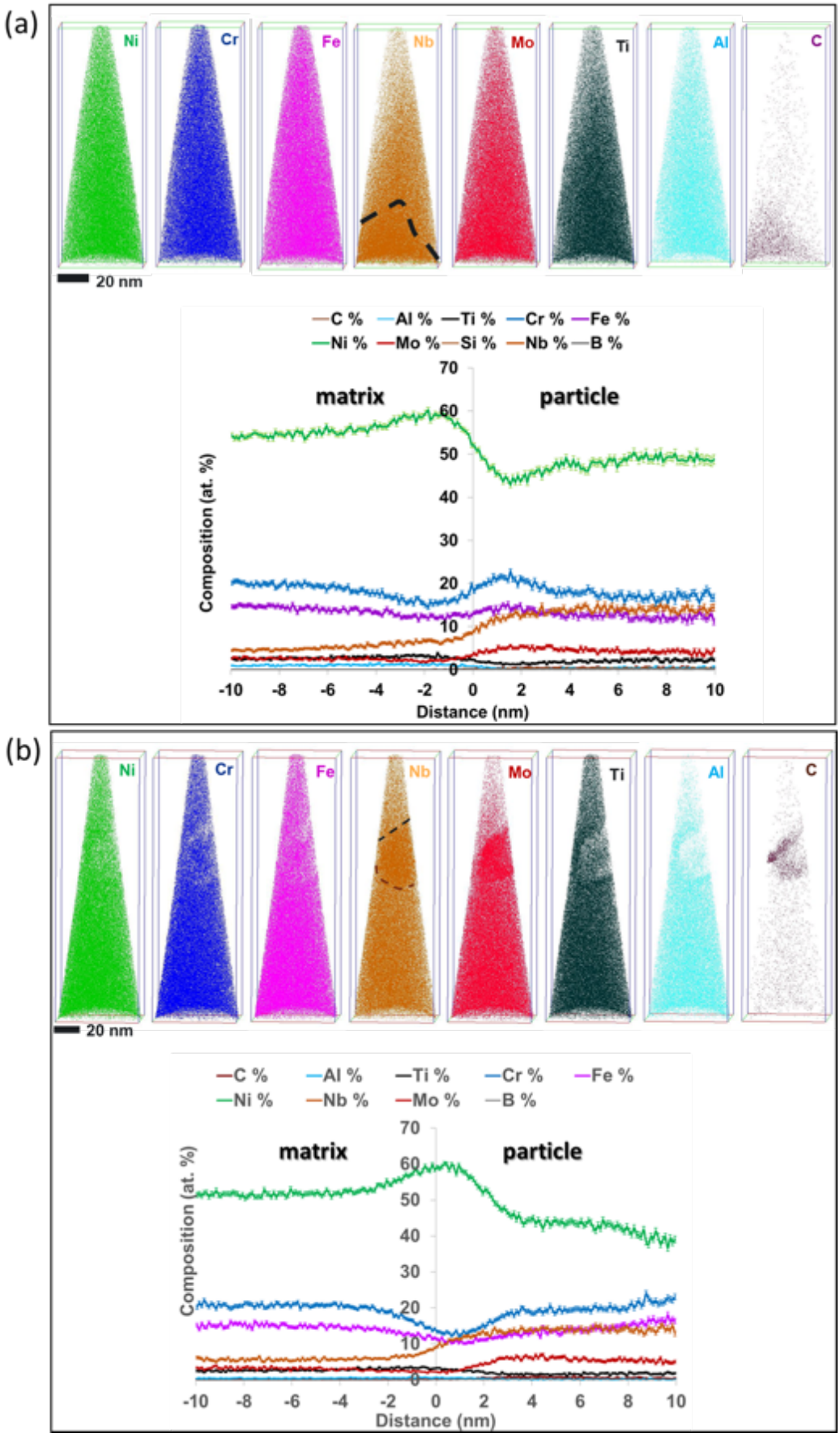

Figure 6. APT 3D reconstruction of the irradiated alloy at 450 °C up to 3 dpa, showing (a) a Fe-Cr-Mo-Nb carbide particle (b) a particle rich in Nb, Mo and C.

3. Discussion

3.1. Effect of temperature and dose on damage evolution

It has been reported that Ni and Ni-based alloys show stacking fault tetrahedra (SFT), ½<110> perfect loops and 1/3<111> faulted Frank loops under irradiation [26]. SFT are reported to form as a result of collapse of vacancy type Frank loops during the collusion cascade [27, 28]. The collapse of Frank loops might result in perfect SFTs with triangle shape, truncated SFTs and vacancy or interstitial type Frank loops. It has been reported that if the tetrahedron is viewed along one out of the six <110> directions, the structure will project to 2D image as a triangular shape, rather than a trapezoidal shape when viewed through the <001> direction [29]. In the present study, defects have been observed along the zone axes of <100> and <110> at the irradiation temperatures of 200 and 450 °C. Even though the defects are mainly found to be dislocation loops, there are some SFTs which are pointed by red arrows in Fig. 7. It should be noted that even though there is no quantitative data, clearly the fraction of SFTs is higher at 200 °C while their size is larger at 450 °C. Ma et al. investigated the defect evolution in pure Ni using in-situ Ni^{2+} irradiation at temperatures between 400 and 700 °C at which mainly dislocation loops formed [30]. Yao et al. found that fraction of SFT decreases with increasing irradiation temperature. They reported an SFT fraction of 39% at room temperature while SFT fraction at 250 °C was only 13% [31]. This was attributed to first transformation of SFT to Frank loops and then the vacancy emission in Ni which was reported to start at 490 K [32, 33]. Moreover, Zhang et al. observed that the size of the SFTs increases with increasing temperature which was attributed to the capture of free vacancies by the SFTs which is more pronounced at high temperatures due to the easier migration of vacancies [34].

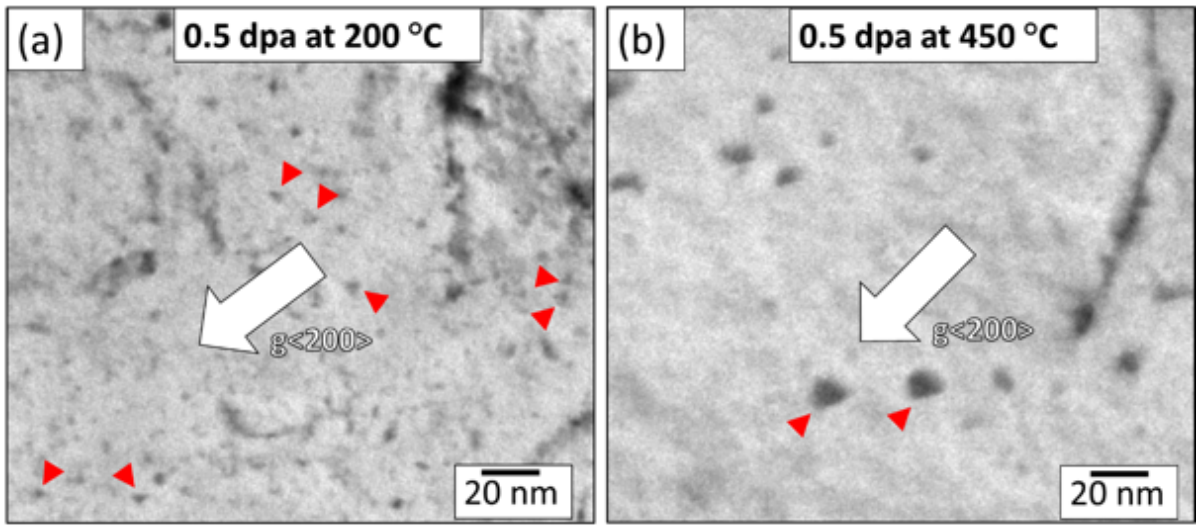

Figure 7. BFTEM micrographs showing the damage after 0.5 dpa (a) 200 °C and (b) 450 °C. Red arrows point the SFTs. Arrows show the g<200> tilted from zone axes of (a) [200] and (b) [110].

The SFTs grow with the absorption of vacancies, and the vacancy migration is reported to start at ~490 K in Nickel [32]. Therefore, the vacancy migration at 200 °C is limited resulting in limited growth of the defects. Therefore, the saturation of defect size at 200 °C in Fig. 5 may indicate that the defects are mostly vacancy-rich defect clusters (SFTs and loops) and interstitial

loops. On the other hand, since the Frank loops are mostly interstitial, the loops have been reported to grow with the absorption of SIAs at the temperatures above 400 °C while SFTs grow with the absorption of vacancies [26, 34].

While the average area of the loops at 200 °C remains at ~17 nm^2 with increasing dose, the size of the loops as a result of 450 °C irradiations increases in a logarithmic fashion at higher doses and reaches ~30 nm^2 at 3 dpa (Fig. 5). Moreover, the areal density of the loops is higher at 200 °C compared to 450 °C. When the thickness of the investigated regions is assumed to be ~100 nm, the number density of the dislocation loops reaches ~$8.8x10^{21}$ m^{-3} or ~$8.8x10^{14}$ m^{-2} and ~$6.2x10^{21}$ m^{-3} or ~$6.2x10^{14}$ m^{-2} after 3 dpa irradiations at 200 °C and 450 °C, respectively. Considering that migration of the defects is promoted at high temperatures, size of the loops becomes larger either by coalescence of the loops or absorption of interstitials. [35]. Zhang et al. conducted in-situ Kr^{2+} irradiations on Inconel X-750 at the temperatures between 60 and 400 °C up to ~2.2 dpa and reported no clear trend in size and density of dislocation loops with temperature [26]. In a separate study, they found that Frank loops would grow between 400 and 500 °C and unfaulting of interstitial Frank loops occurs at 500 and 600 °C. Consequently, the trend indicates an increasing size and decreasing density at high temperatures, similar to this study. [34]. Similarly, Hashimoto et al. performed irradiations on Inconel 718 alloys at 200 °C using various ion probes [36]. They reported that size of the loops increases with irradiation dose and unfaulting of the faulted loops occurs at the temperatures as low as 200 °C. In this study, dislocation loop density has been found to be considerably lower compared to the above stated studies which might attributed the unfaulting of the loops which can escape to the foil surface or coalesce with other loops.

It should be noted that the loop size distribution is closely related to the thickness of the investigated region. Ma et al. reported that the size and density of the loops increase with the foil thickness at different temperatures [30]. They found that there is a critical thickness for the thickness independent analyses which increases with increasing irradiation temperature. For instance, the critical thickness is ~100 nm for 450 °C while it is ~220 nm for 510 °C. We performed irradiations at the thick regions of the foils, therefore, investigations ignore the thickness effect.

3.2. Effect of second phase particles and cellular structure / comparison with other nickel based alloys:

It has been reported that nano-particles enhance the radiation resistance of materials, depending on the size and fraction of the particles. For instance, 14YWT alloy which is a nano-structured ferritic alloy (NFA) having nano-oxide density in the order of 10^{23} m^{-3} shows almost zero swelling and a smaller number of dislocation loops [9]. On the other hand, another oxide dispersion strengthened alloy, MA956, having larger particle size with much lower density shows higher swelling and radiation damage. In this study, particle size is relatively large and

number density is much smaller compared to the NFAs. Recently, it was shown that additively manufactured austenitic and ferritic/martensitic steels have improved mechanical properties as well as radiation resistance. This has been attributed to the cellular structure formation as a result of non-equilibrium cooling [39-41]. Cellular structure which is formed by the pile up of dislocations acts as sink for the defects [40, 41].

Even though most of the studies are concentrated on the pure Nickel, there are few studies on radiation resistance of nickel super alloys. For instance, Zhao et al. conducted ion irradiations on pure Nickel at room temperature and they found that number density of defects is saturated at ~$4x10^{23}$ m^{-3} above 1 dpa [42]. Lear et al. compared the radiation resistance of various ferritic, austenitic and Nickel based alloys irradiated with dual ions up to 150 dpa and ~13 appm/He at 400 °C [43]. They reported the loop density as $1.3x10^{22}$ m^{-3} in Inconel 718 alloy. Moreover, Hashimoto et al. performed triple beam irradiation on Inconel 718 at 200 °C to 10 dpa and reported a loop density of $2x10^{22}$ m^{-3} [36]. Zhang et al. conducted in-situ Kr^{2+} irradiations on Inconel X-750 at the temperatures between 60 and 400 °C [26]. They observed that at ~2.2 dpa, number density of the loops is ~$2x10^{15}$ m^{-2} at 500 °C and ~$3x10^{15}$ m^{-2} at 400 °C while it is ~$3.5x10^{15}$ m^{-2} at 200 °C. In this study, when the thickness of the investigated regions is assumed to be ~100 nm, the number density of the dislocation loops reaches ~$8.8x10^{21}$ m^{-3} or ~$8.8x10^{14}$ m^{-2} and ~$6.2x10^{21}$ m^{-3} or ~$6.2x10^{14}$ m^{-2} after 3 dpa irradiations at 200 °C and 450 °C, respectively. These numbers can be tuned further as the current analysis does not include 1/3 of the perfect loops. Yao et al. found that fraction of SFT decreases with increasing irradiation temperature [31]. They reported an SFT fraction of 39% at room temperature while SFT fraction at 250 °C was only 13%. Based on this information and our observations in Fig. 7, it is reasonable to assume the fraction of SFTs as ~15% and ignore the SFTs at 450 °C. Moreover, 1/3 of the perfect loops are missing from the measurements. Considering the SFTs and the missing dislocations, defect density vs. dose plots can be modified as seen in Fig. 8. The number density of the dislocation loops is found as ~$1.1x10^{22}$ m^{-3} and ~$7.8x10^{21}$ m^{-3} after 3 dpa irradiations at 200 °C and 450 °C, respectively. Apparently, the number density of the defects is 2-40 times lower compared to the above stated studies. This can be attributed to (1) the improved radiation resistance due to the existence of second phase particles and cellular structure as a result of additive manufacturing (2) under estimation of the loop density due to the escape of the loops to the foil surfaces.

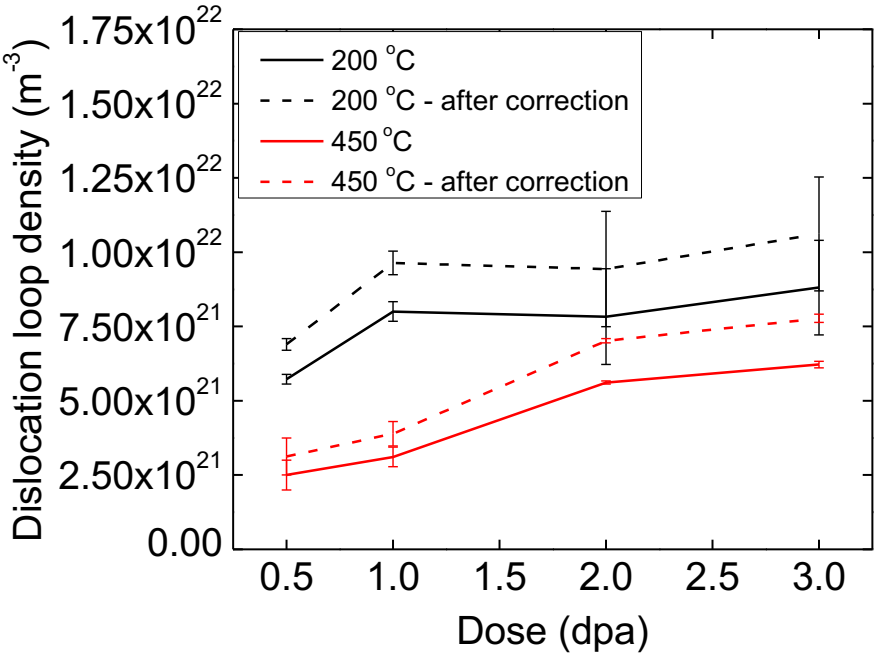

Figure 8. Dislocation loop density vs. dose plot before and after including the invisible portion of perfect loops.

In order to understand how much improvement occurs due to the existence of both second phase particles and the cell structure, sink strength of the structures, namely second phase particles, dislocations cell boundaries and free surfaces can be calculated. The sink strength of the dislocations can be calculated by $k_{disl}^2 = z_d\rho_d$ where z_d is the atomic sites for defect (both interstitials and vacancies) capture per dislocation line intercepted with a crystal plane (~2-10) and ρ_d is dislocation density [44]. Dislocation density has been measured to be ~2.5x10^{14} m^{-2} from the grains in two beam condition on the micrographs taken in multi-beam condition (see Fig.9a). Therefore, k_{disl}^2 can be taken as the dislocation density ~2.5x10^{14} m^{-2} [44]. It should be noted that the edge dislocations are biased towards interstitials which becomes more pronounced with an increasing dislocation density [45].

The sink strength for the second phase particles, k_{sp}^2, can be calculated as $k_{sp}^2 = 4\pi R\rho Y$ where R and ρ are the radius and number density of the particles and Y is a constant related to the bias for vacancy and interstitial trapping, which is reported to be ~1 [46-48]. The size and number density of the particles have been measured as 22.5±1.5 nm and 6.0±0.9x10^{20} m^{-3}, respectively (see Fig. 9b and c). k_{sp}^2 thus, is calculated as 1.7x10^{14} m^{-2}.

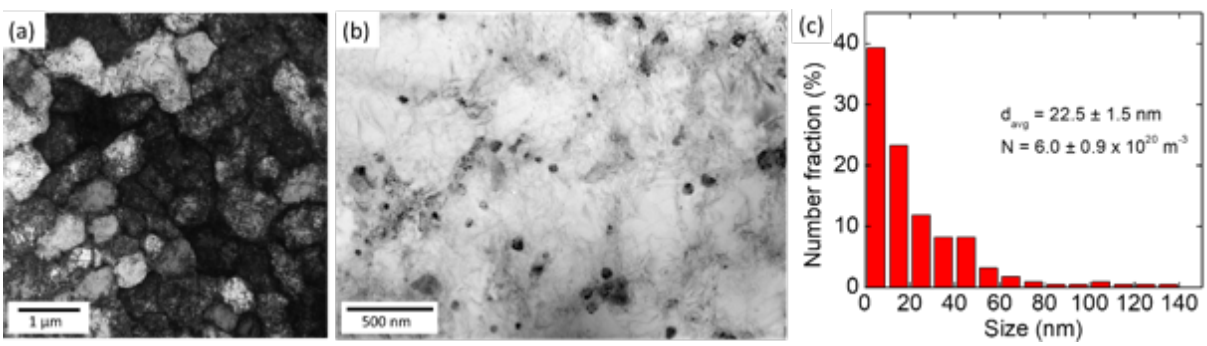

Figure 9. BFTEM micrograph (a) in multi-beam condition showing the cells with different orientations (b) showing the second phase particle distribution (c) the second phase particle size distribution plot.

Fig. 10 shows that the fraction of low angle boundaries (cell boundaries) with a misorientation angle less than 5° is ~95%. The sink strength of the high angle grain boundaries and low angle cell boundaries should be considered separately. In ferritic nanostructured alloys, we have shown that sink efficiency of the high angle grain boundaries is much higher compared to the grain boundaries with misorientation angle of <5° [10, 49]. On the other hand, Kedharnath et al. has reported that the low angle grain boundaries have higher sink efficiency compared to the high angle grain boundaries in α-Fe [50]. Similarly, Moladje et al. investigated the sink strength and bias of low angle symmetric tilt boundaries in Ni [45]. They found that if the distance between dislocations (or inter-spacing - d) is less than 30 nm, there is strong elastic interactions creating a strong bias for vacancies and dumbbells. If d>30 nm, they act as neutral continuous planar sinks where sink density can be represented by $k^2 = 12/(d-e)^2$ [51], *e* being the width of the planar sink which is typically around ~0.5 nm for undeformed materials [52]. In this study, symmetry of the tilt angle boundaries is not known, nor the inter-spacings. However, even though the average interspacing is considered more than 30 nm, k_{cb}^2, the sink strength of cell boundaries, can be calculated as more than 10^{15} m^{-2}.

The average grain size bounded by high angle grain boundaries in Fig.1b is ~20 μm and sink strength for grain boundaries, k_{gb}^2, can be calculated by [53, 54];

$$k_{gb}^2 = 6k/d \text{ when } kd \rightarrow \infty \qquad \text{Eq. 1}$$

$$k_{gb}^2 = 60/d^2 \text{ when } kd \rightarrow 0 \qquad \text{Eq. 2}$$

where *d* is the diameter of the grains, k^2 is the sink strength of the other internal sinks which are second phase particles, dislocations and cell boundaries. *kd* can be calculated as >630, thus, Eq. 1 can be used, and sink strength for grain boundaries can be calculated as ~10^{13} m^{-2}.

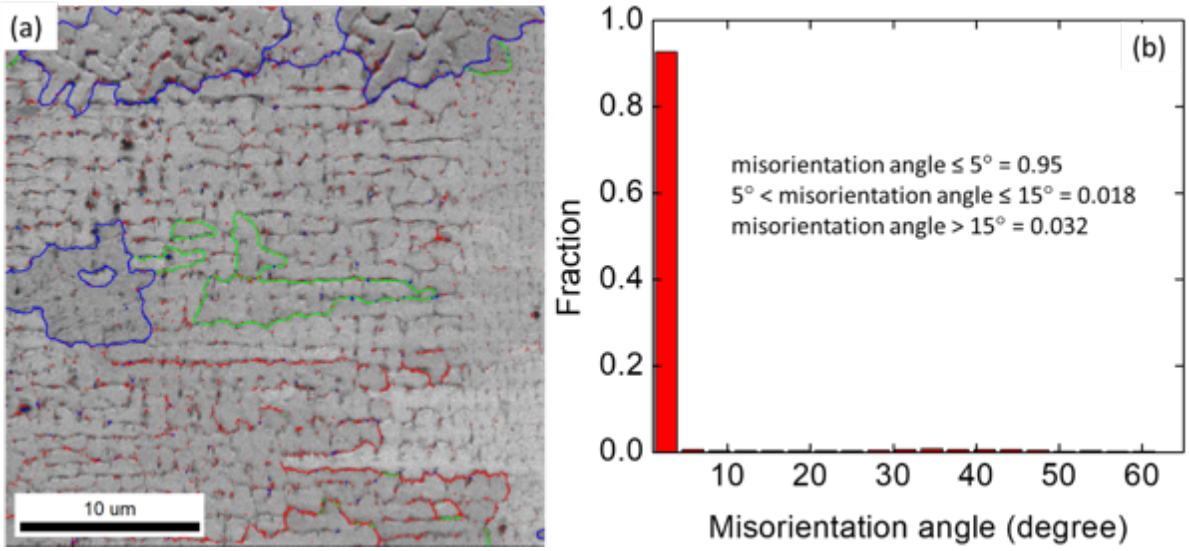

Figure 10. (a) Gray scale EBSD map showing the distribution of misorientation angle of grain boundaries (b) plot of misorientation angle fractions. In (a) blue color represents high angle

grain boundaries (>15°); green color represents grain boundaries with misorientation angle between 5° and 15°; red color represents grain boundaries with misorientation angle between 1° and 5°.

Free surfaces in thin films, such as TEM foils, can also act as sinks under irradiation [55]. The sink strength of the free surfaces in thin foils, k_s^2, can be calculated by [53];

$$k_s^2 = k_a/l \text{ when } k_a l \rightarrow \infty \quad \text{Eq. 3}$$

$$k_s^2 = 3/l^2 \text{ when } k_a l \rightarrow 0 \quad \text{Eq. 4}$$

where k_a^2 is the sink strength of all other microstructural defect sinks within the foil (second phase particles, dislocations, cell and grain boundaries), which is $>10^{15}$ m^{-2}, and l is the half of the foil thickness, which is ~50 nm. $k_a l$ can be calculated as >1.6 and using Eq. 4, k_s^2 is calculated as 1.2×10^{15} m^{-2}.

When the sink strengths are compared, cell boundaries and the foil surfaces are the predominant defect sinks. However, since grain boundary area to surface ratio is high in the case of nano-structured alloys, surface effect should be much less than the calculated value as discussed by El-Atwani et al. [37]. Furthermore, if the average distance between the dislocations is less than 30 nm, considering the sink bias of the cell boundaries, they act as the main sinks in this material. Second phase particles have small amount of contribution to the defect removal. However, since they precipitate mostly at the cell boundaries, cell boundaries are stabilized by these particles which indicates the indirect contribution of these particles. It should be noted that for the effective removal of the defects, number density and size are crucial, as shown in Ref [7]. Moreover, when the sink bias of the dislocations is considered, they will be more effective on removing the interstitials more than the calculated strength due to dislocations.

3.3. Radiation effects on composition:

Radiation has been shown to result in segregation at the dislocation and dislocation loops, segregation/depletion at the grain boundaries and formation of second phase particles at high temperatures [10, 49]. In nickel-based alloys, Song et al. and Lear et al. reported that γ' and γ'' particles either dissolve or become disordered while some Ni-rich second phase particles precipitate [43, 56, 57]. In this study, the matrix composition is homogenous before and after irradiation as seen in Fig. 11, indicating the lack of formation of any new nanoscale second phase precipitation and segregation on the defects within the matrix.

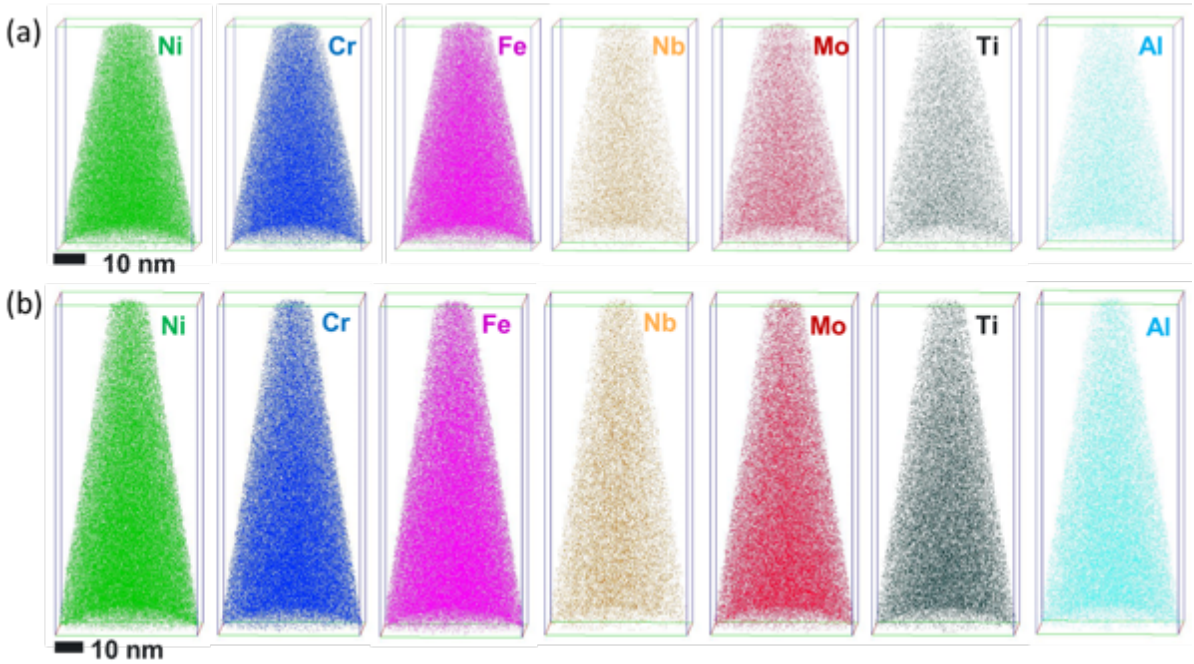

Figure 11. APT 3D reconstruction of the matrix in (a) as-built and (b) Kr ion irradiated alloy at 450 °C up to 3 dpa, showing the elemental distribution in the matrix.

Table 2 indicates that there is no considerable change in composition of matrix after 3 dpa of irradiation at 450 °C. However, Ti amount seems to increase slightly while Nb decreases at the matrix. Initially, these changes can be thought to occur due to the segregation/depletion at the grain/cell boundaries which is explained by either inverse Kirkendall mechanism or solute size effects [57, 58]. Toijer et al. have shown that Ti diffusion occurs through vacancies in nickel matrix indicating an inverse Kirkendall mechanism [59]. Moreover, Ti is an oversized atom in Nickel matrix and therefore it prefers to diffuse through vacancies resulting in depletion at the grain boundaries which also explains the increased amount of Ti at the matrix. On the other hand, diffusion coefficient of Nb in Nickel matrix and atomic size are similar to those of Ti [47, 60]. Thus, Nb depletion is expected at the grain boundaries which leads to matrix enrichment of Nb. However, decrease in Nb amount cannot be explained by RIS. This can be attributed to a small variation in the composition of Nb-containing second phase particles.

Table 2. Elemental distribution in the matrix of the alloy in as-built and irradiated conditions measured using APT.

	As-built		**Irradiated**	
Element	**At. %**	**Error**	**At. %**	**Error**
Ni	54.78	0.072	54.63	0.052
Cr	21.75	0.040	21.87	0.029
Fe	17.93	0.036	17.84	0.026
Mo	1.78	0.011	1.76	0.008
Al	1.10	0.008	1.11	0.006
Ti	1.08	0.008	1.28	0.006
Nb	0.88	0.007	0.66	0.005

Si	0.04	0.002	0.04	0.001
O	0.02	0.001	0.02	0.001
Mn	0.02	0.001	0.02	0.001
V	0.01	0.001	0.02	0.001
C	0.01	0.001	0.01	0.001

Conclusion:

In this study, composition of the IN-718 alloys has been modified to obtain second phase particles and these alloys were produced using laser powder bed fusion technique. It has been shown that the microstructure consists of dislocation cells with an average size of ~500 nm within large grains of ~20 μm. The misorientation angle between the cells is less than 5° while grain boundaries are mostly high angle grain boundaries with misorientation angle larger than 15°. There are also second phase particles of Mo-Nb-Ti-(V) rich MC type carbides and Laves phase; Y-O, Y-(Ti)-Al-O; Fe-Cr-Mo-Nb-Ti-Al-V particles. The size and number density of particles (<150 nm) is determined as 22.5±1.5 nm and $6.0\pm0.9 \times 10^{20}$ m^{-3}.

In-situ irradiations have been conducted at 200 and 450 °C up to 3 dpa. Effect of dose and temperature on the defect evolution and composition have been investigated using transmission electron microscopy and atom probe tomography techniques. It has been found that SFTs, faulted loops and perfect loops are formed at both 200 °C and 450 °C whereas SFT fraction decreases considerably at 450 °C. While defect density increases with dose at both 200 °C and 450 °C, defect size remains constant at 200 °C and increases at 450 °C. This infers that the fraction of vacancy type defects (SFTs and loops) is high and therefore, their migration is limited at 200 °C. On the other hand, dislocation loops are the main defects and they are presumed to be mostly interstitial type at 450 °C. Furthermore, irradiation at 450 °C does not cause any change in composition of both matrix and the particles except small variations in Ti and Nb content. This has been attributed to radiation induced segregation/depletion at the grain/cell boundaries or particle/matrix interface. Overall, the radiation resistance of this novel alloy has been shown to surpass other nickel alloys due to the existence of cell boundaries stabilized by the second phase particles as a result of additive manufacturing.

Acknowledgements

This work was supported by the U.S. Department of Energy, Office of Nuclear Energy under DOE Idaho Operations Office Contract DE-AC07- 051D14517 as part of a Nuclear Science User Facilities experiment (CCN:245543). AD would like to acknowledge the support from the PNNL Open call Laboratory directed research and development program. The APT sample preparation and APT analysis was performed using facilities at the Environmental Molecular Sciences Laboratory, a national scientific user facility sponsored by the DOE's Office of Biological and Environmental Research and located at Pacific Northwest National Laboratory (PNNL). O.E. acknowledges support from the Laboratory Directed Research and Development program of Los Alamos National Laboratory under the early career program project number 20210626ECR.

References:

[1] X. Li, J.J. Shi, C.H. Wang, G.H. Cao, A.M. Russell, Z.J. Zhou, C.P. Li, G.F. Chen, Effect of heat treatment on microstructure evolution of Inconel 718 alloy fabricated by selective laser melting, Journal of Alloys and Compounds, 764 (2018) 639-649.
[2] A.F. Rowcliffe, L.K. Mansur, D.T. Hoelzer, R.K. Nanstad, Perspectives on radiation effects in nickel-base alloys for applications in advanced reactors, Journal of Nuclear Materials, 392 (2009) 341-352.
[3] X. Wang, X. Gong, K. Chou, Review on powder-bed laser additive manufacturing of Inconel 718 parts, Proceedings of the Institution of Mechanical Engineers, Part B: Journal of Engineering Manufacture, 231 (2016) 1890-1903.
[4] T. Liu, E.R. Reese, I. Ghamarian, E.A. Marquis, Atom probe tomography characterization of ion and neutron irradiated Alloy 800H, Journal of Nuclear Materials, 543 (2021) 152598.
[5] B.H. Sencer, G.M. Bond, F.A. Garner, M.L. Hamilton, S.A. Maloy, W.F. Sommer, Correlation of radiation-induced changes in mechanical properties and microstructural development of Alloy 718 irradiated with mixed spectra of high-energy protons and spallation neutrons, Journal of Nuclear Materials, 296 (2001) 145-154.
[6] C. Sun, M. Kirk, M. Li, K. Hattar, Y. Wang, O. Anderoglu, J. Valdez, B.P. Uberuaga, R. Dickerson, S.A. Maloy, Microstructure, chemistry and mechanical properties of Ni-based superalloy Rene N4 under irradiation at room temperature, Acta Materialia, 95 (2015) 357-365.
[7] E. Aydogan, O. El-Atwani, M. Li, S.A. Maloy, In-situ observation of nano-oxide and defect evolution in 14YWT alloys, Materials Characterization, 170 (2020) 110686.
[8] E. Aydogan, N. Almirall, G.R. Odette, S.A. Maloy, O. Anderoglu, L. Shao, J.G. Gigax, L. Price, D. Chen, T. Chen, F.A. Garner, Y. Wu, P. Wells, J.J. Lewandowski, D.T. Hoelzer, Stability of nanosized oxides in ferrite under extremely high dose self ion irradiations, Journal of Nuclear Materials, 486 (2017) 86-95.
[9] E. Aydogan, S.A. Maloy, O. Anderoglu, C. Sun, J.G. Gigax, L. Shao, F.A. Garner, I.E. Anderson, J.J. Lewandowski, Effect of tube processing methods on microstructure, mechanical properties and irradiation response of 14YWT nanostructured ferritic alloys, Acta Materialia, 134 (2017) 116-127.
[10] E. Aydogan, J.S. Weaver, U. Carvajal-Nunez, M.M. Schneider, J.G. Gigax, D.L. Krumwiede, P. Hosemann, T.A. Saleh, N.A. Mara, D.T. Hoelzer, B. Hilton, S.A. Maloy, Response of 14YWT alloys under neutron irradiation: A complementary study on microstructure and mechanical properties, Acta Materialia, 167 (2019) 181-196.
[11] C.W. Park, J.M. Byun, W.J. Choi, S.Y. Lee, Y.D. Kim, Improvement of high temperature mechanical properties of Ni-based oxide dispersion strengthened alloys by preferential formation of Y-Ti-O complex oxide, Materials Science and Engineering: A, 740-741 (2019) 363-367.
[12] E. Aydogan, O. El-Atwani, S. Takajo, S.C. Vogel, S.A. Maloy, High temperature microstructural stability and recrystallization mechanisms in 14YWT alloys, Acta Materialia, 148 (2018) 467-481.
[13] E. Aydogan, C.J. Rietema, U. Carvajal-Nunez, S.C. Vogel, M. Li, S.A. Maloy, Effect of High-Density Nanoparticles on Recrystallization and Texture Evolution in Ferritic Alloys, Crystals, 9 (2019).
[14] Y.B. Chun, X. Mao, C.H. Han, J. Jang, Microstructural evolution and tensile properties of oxide dispersion strengthened Alloy 617 at elevated temperatures, Materials Science and Engineering: A, 706 (2017) 161-171.
[15] D.T. Hoelzer, J. Bentley, M.A. Sokolov, M.K. Miller, G.R. Odette, M.J. Alinger, Influence of particle dispersions on the high-temperature strength of ferritic alloys, Journal of Nuclear Materials, 367–370, Part A (2007) 166-172.
[16] B. Graybill, M. Li, D. Malawey, C. Ma, J.-M. Alvarado-Orozco, E. Martinez-Franco, Additive Manufacturing of Nickel-Based Superalloys, in, 2018.
[17] S. Bagherifard, G. Roscioli, M.V. Zuccoli, M. Hadi, G. D'Elia, A.G. Demir, B. Previtali, J. Kondás, M. Guagliano, Cold Spray Deposition of Freestanding Inconel Samples and Comparative Analysis with Selective Laser Melting, Journal of Thermal Spray Technology, 26 (2017) 1517-1526.
[18] S. Bagherifard, S. Monti, M.V. Zuccoli, M. Riccio, J. Kondás, M. Guagliano, Cold spray deposition for additive manufacturing of freeform structural components compared to selective laser melting, Materials Science and Engineering: A, 721 (2018) 339-350.
[19] R.B. Rebak, X. Lou, Using Additive Manufacturing for Making Light Water Reactor Components, in, 2019.

[20] P. Chen, C. Yang, S. Li, M.M. Attallah, M. Yan, In-situ alloyed, oxide-dispersion-strengthened CoCrFeMnNi high entropy alloy fabricated via laser powder bed fusion, Materials & Design, 194 (2020) 108966.
[21] C. Qiu, A new approach to synthesise high strength nano-oxide dispersion strengthened alloys, Journal of Alloys and Compounds, 790 (2019) 1023-1033.
[22] L. Tan, G. Wang, Y. Guo, Q. Fang, Z. Liu, X. Xiao, W. He, Z. Qin, Y. Zhang, F. Liu, L. Huang, Additively manufactured oxide dispersion strengthened nickel-based superalloy with superior high temperature properties, Virtual and Physical Prototyping, 15 (2020) 555-569.
[23] Y. Shi, Z. Lu, L. Yu, R. Xie, Y. Ren, G. Yang, Microstructure and tensile properties of Zr-containing ODS-FeCrAl alloy fabricated by laser additive manufacturing, Materials Science and Engineering: A, 774 (2020) 138937.
[24] A. Devaraj, D.E. Perea, J. Liu, L.M. Gordon, T.J. Prosa, P. Parikh, D.R. Diercks, S. Meher, R.P. Kolli, Y.S. Meng, S. Thevuthasan, Three-dimensional nanoscale characterisation of materials by atom probe tomography, International Materials Reviews, 63 (2018) 68-101.
[25] O. El-Atwani, E. Esquivel, M. Efe, E. Aydogan, Y.Q. Wang, E. Martinez, S.A. Maloy, Loop and void damage during heavy ion irradiation on nanocrystalline and coarse grained tungsten: Microstructure, effect of dpa rate, temperature, and grain size, Acta Materialia, 149 (2018) 206-219.
[26] H.K. Zhang, Z. Yao, C. Judge, M. Griffiths, Microstructural evolution of CANDU spacer material Inconel X-750 under in situ ion irradiation, Journal of Nuclear Materials, 443 (2013) 49-58.
[27] M.A. Kirk, I.M. Robertson, M.L. Jenkins, C.A. English, T.J. Black, J.S. Vetrano, The collapse of defect cascades to dislocation loops, Journal of Nuclear Materials, 149 (1987) 21-28.
[28] S. Kojima, Y. Sano, T. Yoshiie, N. Yoshida, M. Kiritani, Conversion of stacking fault tetrahedra to voids in electron irradiated Fe-Cr-Ni, Journal of Nuclear Materials, 141-143 (1986) 763-766.
[29] Z. Yao, The relationship between the irradiation induced damage and the mechanical properties of single crystal Ni, in: Ph. D thesis, EPFL, 2005.
[30] K. Ma, B. Décamps, A. Fraczkiewicz, T. Jourdan, F. Prima, M. Loyer-Prost, Free surface impact on radiation damage in pure nickel by in-situ self-ion irradiation: can it be avoided?, Acta Materialia, 212 (2021) 116874.
[31] Z. Yao, R. Schäublin, M. Victoria, The microstructure and tensile properties of pure Ni single crystal irradiated with high energy protons, Journal of Nuclear Materials, 307-311 (2002) 374-379.
[32] A. Bartels, F. Dworschak, M. Weigert, Isochronal recovery and damage rate measurements in dilute NiSi alloys, Journal of Nuclear Materials, 137 (1986) 130-138.
[33] B.N. Singh, S.I. Golubov, H. Trinkaus, D.J. Edwards, M. Eldrup, Review: Evolution of stacking fault tetrahedra and its role in defect accumulation under cascade damage conditions, Journal of Nuclear Materials, 328 (2004) 77-87.
[34] H.K. Zhang, Z. Yao, M.R. Daymond, M.A. Kirk, Elevated temperature irradiation damage in CANDU spacer material Inconel X-750, Journal of Nuclear Materials, 445 (2014) 227-234.
[35] A.K. Koul, R. Castillo, K. Willett, Creep life predictions in nickel-based superalloys, Materials Science and Engineering, 66 (1984) 213-226.
[36] N. Hashimoto, J.D. Hunn, T.S. Byun, L.K. Mansur, Microstructural analysis of ion-irradiation-induced hardening in inconel 718, Journal of Nuclear Materials, 318 (2003) 300-306.
[37] O. El-Atwani, E. Esquivel, E. Aydogan, E. Martinez, J.K. Baldwin, M. Li, B.P. Uberuaga, S.A. Maloy, Unprecedented irradiation resistance of nanocrystalline tungsten with equiaxed nanocrystalline grains to dislocation loop accumulation, Acta Materialia, 165 (2019) 118-128.
[38] P. Xiu, Y.N. Osetsky, L. Jiang, G. Velisa, Y. Tong, H. Bei, W.J. Weber, Y. Zhang, L. Wang, Dislocation loop evolution and radiation hardening in nickel-based concentrated solid solution alloys, Journal of Nuclear Materials, 538 (2020) 152247.
[39] Y.M. Wang, T. Voisin, J.T. McKeown, J. Ye, N.P. Calta, Z. Li, Z. Zeng, Y. Zhang, W. Chen, T.T. Roehling, R.T. Ott, M.K. Santala, Philip J. Depond, M.J. Matthews, A.V. Hamza, T. Zhu, Additively manufactured hierarchical stainless steels with high strength and ductility, Nature Materials, 17 (2018) 63-71.

[40] Z. Shang, C. Fan, S. Xue, J. Ding, J. Li, T. Voisin, Y.M. Wang, H. Wang, X. Zhang, Response of solidification cellular structures in additively manufactured 316 stainless steel to heavy ion irradiation: an in situ study, Materials Research Letters, 7 (2019) 290-297.
[41] S. Li, J. Hu, W.-Y. Chen, J. Yu, M. Li, Y. Wang, Evolution of cellular dislocation structures and defects in additively manufactured austenitic stainless steel under ion irradiation, Scripta Materialia, 178 (2020) 245-250.
[42] X. Zhao, D.J. Strickland, P.M. Derlet, M.-r. He, Y.-J. Cheng, J. Pu, K. Hattar, D.S. Gianola, In situ measurements of a homogeneous to heterogeneous transition in the plastic response of ion-irradiated 〈111〉 Ni microspecimens, Acta Materialia, 88 (2015) 121-135.
[43] C.R. Lear, M. Song, M. Wang, G.S. Was, Dual ion irradiation of commercial and advanced alloys: Evaluating microstructural resistance for high dose core internals, Journal of Nuclear Materials, 516 (2019) 125-134.
[44] M. Song, Y.D. Wu, D. Chen, X.M. Wang, C. Sun, K.Y. Yu, Y. Chen, L. Shao, Y. Yang, K.T. Hartwig, X. Zhang, Response of equal channel angular extrusion processed ultrafine-grained T91 steel subjected to high temperature heavy ion irradiation, Acta Materialia, 74 (2014) 285-295.
[45] G.F. Bouobda Moladje, L. Thuinet, C. Domain, C.S. Becquart, A. Legris, Phase-field calculations of sink strength in Al, Ni, and Fe: A detailed study of elastic effects, Computational Materials Science, 183 (2020) 109905.
[46] G.S. Was, Fundamentals of Radiation Materials Science: Metals and Alloys citation, Springer, 2016.
[47] M. Song, Y. Yang, M. Wang, W. Kuang, C.R. Lear, G.S. Was, Probing long-range ordering in nickel-base alloys with proton irradiation, Acta Materialia, 156 (2018) 446-462.
[48] A.D. Brailsford, R. Bullough, The rate theory of swelling due to void growth in irradiated metals, Journal of Nuclear Materials, 44 (1972) 121-135.
[49] E. Aydogan, E. Martinez, K. March, O. El-Atwani, D.L. Krumwiede, P. Hosemann, T. Saleh, S.A. Maloy, α' formation kinetics and radiation induced segregation in neutron irradiated 14YWT nanostructured ferritic alloys, Scientific Reports, 9 (2019) 8345.
[50] A. Kedharnath, R. Kapoor, A. Sarkar, Atomistic simulation of interaction of collision cascade with different types of grain boundaries in α-Fe, Journal of Nuclear Materials, 523 (2019) 444-457.
[51] C. Jiang, N. Swaminathan, J. Deng, D. Morgan, I. Szlufarska, Effect of Grain Boundary Stresses on Sink Strength, Materials Research Letters, 2 (2014) 100-106.
[52] D. Prokoshkina, V.A. Esin, G. Wilde, S.V. Divinski, Grain boundary width, energy and self-diffusion in nickel: Effect of material purity, Acta Materialia, 61 (2013) 5188-5197.
[53] R. Bullough, M.R. Hayns, M.H. Wood, Sink strengths for thin film surfaces and grain boundaries, Journal of Nuclear Materials, 90 (1980) 44-59.
[54] L.K. Mansur, Theory and experimental background on dimensional changes in irradiated alloys, Journal of Nuclear Materials, 216 (1994) 97-123.
[55] M. Li, M.A. Kirk, P.M. Baldo, D. Xu, B.D. Wirth, Study of defect evolution by TEM with in situ ion irradiation and coordinated modeling, Philosophical Magazine, 92 (2012) 2048-2078.
[56] M. Song, C.R. Lear, C.M. Parish, M. Wang, G.S. Was, Radiation tolerance of commercial and advanced alloys for core internals: a comprehensive microstructural characterization, Journal of Nuclear Materials, 510 (2018) 396-413.
[57] A.D. Marwick, Segregation in irradiated alloys: The inverse Kirkendall effect and the effect of constitution on void swelling, Journal of Physics F: Metal Physics, 8 (1978) 1849-1861.
[58] L.E. Rehn, P.R. Okamoto, D.I. Potter, H. Wiedersich, Effect of solute misfit and temperature on irradiation-induced segregation in binary Ni alloys, Journal of Nuclear Materials, 74 (1978) 242-251.
[59] E. Toijer, L. Messina, C. Domain, J. Vidal, C.S. Becquart, P. Olsson, Solute-point defect interactions, coupled diffusion, and radiation-induced segregation in fcc nickel, Physical Review Materials, 5 (2021) 013602.
[60] J.D. Tucker, Solute-Vacancy Interactions in Nickel, MRS Online Proceedings Library, 1645 (2014) 808.